International Journal of Geo-Information

MDPI

Article

Potential of UAVs for Monitoring Mudflat Morphodynamics (Application to the Seine Estuary, France)

Marion Jaud [1,*], Florent Grasso [2], Nicolas Le Dantec [1,3], Romaric Verney [2], Christophe Delacourt [1], Jérôme Ammann [1], Julien Deloffre [4] and Philippe Grandjean [5]

1 Domaines Océaniques - UMR 6538, Université de Bretagne Occidentale, IUEM, Technopôle Brest-Iroise, Rue Dumont D'Urville, F-29280 Plouzané, France; nicolas.ledantec@univ-brest.fr (N.L.D.); christophe.delacourt@univ-brest.fr (C.D.); jerome.ammann@univ-brest.fr (J.A.)

2 Ifremer - Dyneco/Physed - Centre de Bretagne, BP 70, F-29280 Plouzané, France; Florent.Grasso@ifremer.fr (F.G.); Romaric.Verney@ifremer.fr (R.V.)

3 CEREMA - Centre d'Etudes et d'expertise sur les Risques, l'Environnement, la Mobilité et l'Aménagement, DTechEMF, F-29280 Plouzané, France

4 Université de Rouen, M2C, UMR 6143, CNRS, Morphodynamique Continentale et Côtière, F-76821 Mont Saint Aignan Cedex, France; julien.deloffre@univ-rouen.fr

5 Laboratoire de Géologie de Lyon - UMR 5276, Université Claude Bernard Lyon 1, Campus de la Doua, 2 rue Raphaël Dubois, F-69622 Villeurbanne Cedex, France; philippe.grandjean@univ-lyon1.fr

* Correspondence: marion.jaud@univ-brest.fr; Tel.: +33-298-498-891

Academic Editors: Gonzalo Pajares Martinsanz and Wolfgang Kainz
Received: 23 November 2015; Accepted: 8 April 2016; Published: 13 April 2016

Abstract: Intertidal mudflats play a critical role in estuarine exchange, connecting marine and continental supplies of nutrients and sediments. However, their complex morphodynamics, associated with a wide range of physical and biological processes, are still poorly understood and require further field investigation. In addition, mudflats are challenging areas for Structure-from-Motion (SfM) photogrammetric surveys. Indeed, the mudflats generally hold back residual tidal water, which can make stereo restitution particularly difficult because of poor correlations or sun-glint effects. This study aims to show the potential of light UAVs (Unmanned Aerial Vehicles) for monitoring sedimentary hydrodynamics at different spatial scales in a silty estuary. For each UAV mission an orthophotograph and a Digital Elevation Model (DEM) are computed. From repeated surveys the diachronic evolution of the area can be observed via DEM differencing. Considering the ground texture in such a context, the stereo restitution process is made possible because of the high spatial resolution of the UAV photographs. Providing a synoptic view as well as high spatial resolution (less than 4 cm), the UAV dataset enables multi-scale approaches from the study of large areas to the morphodynamics of smaller-scale sedimentary structures and the morphodynamics impact of plant ground cover.

Keywords: coastal monitoring; Unmanned Aerial Vehicle; photogrammetry; estuary; mudflat areas; morphological features

1. Introduction

Estuaries represent specific environments, mixing continental fresh and marine salty waters, associated with rich biodiversity and ecological services. Moreover, they are favored places for social and economic developments. Estuarine systems are complex and composed of different interconnected areas, usually including a main channel, ebb tidal delta banks, and lateral mudflats. Intertidal mudflats are a key feature within the complex estuarine ecosystem. The lateral, mixed sediment

(clays, silts, sands) banks of the main channel, which are successively flooded and uncovered by tides and/or river discharge variations, play an important role in estuary sediment dynamics as a temporary sediment source or sink (e.g., [1,2]). Mudflats are the interface between the flood plain and the main river channel, and are characterized by a cross-shore slope (either steep or smooth), usually separated into two specific environments: the shore, located in the upper part of the mudflat and flooded during high spring tides; and the tidal flat, the lower part of the mudflat, with an upper limit corresponding to the highest sea level reached during the mean tidal ranges. Shores are mainly colonized with halophile (salt-tolerant) vegetation, when vegetation is present, while the tidal flat can either be bare or colonized by vegetation in its upper part at the transition to the shore. Ridge/runnel and meandering tidal creeks perpendicular to the main channel are also a typical feature of intertidal mudflats, identified as preferential exchange pathways for sediment and water between the flood plain, shore, tidal flat, and main channel. Hydrodynamic conditions (currents, bed shear stress) in all parts of the system affect the development of vegetation, but, conversely, the presence of vegetation can also affect the hydrodynamics (e.g., reduction of current velocity, turbulence decrease [3]), leading to changes in sediment dynamics (e.g., erosion/deposition [4,5]).

Hydrological (river discharge and continental suspended solid inputs), meteorological (wind, wave), and hydrodynamic (tide) forcing factors control estuarine sediment dynamics, and hence mudflat morphodynamics, at different time scales: from hours (tides), days (storm events), fortnightly cycles (neap/spring tides), and seasons (river discharges) to decades (changes in land use, anthropogenic stream alteration) and centuries (climate change). Morphological changes are associated with either erosion/deposition events leading to mudflat bed elevation changes, or tidal creek development and/or migration. Tidal forcing and storms result in millimeters to centimeters of bed elevation changes [6] and the formation of bedforms (*i.e.*, ripples). Changes occurring at moderate temporal scales are associated with centimeter to decimeter variations, while slow, long-term variability is potentially associated with mudflat retreat or progradation, *i.e.*, decimeter to meter changes. These changes are not generally applied homogeneously across the mudflat but are expressed with strong spatial variability. Finally, the aforementioned physical processes driving mudflat morphodynamics interact directly with vegetation ground cover.

Reflecting such a complex environment, the macrotidal Seine Estuary (maximum tidal range of 8.0 m at its mouth) is located in the northwestern part of France (Figure 1). It is one of the largest estuaries on the Northwestern European continental shelf, with a catchment area of more than 79,000 km^2. The mean annual Seine River flow, computed over the last 50 years, is 450 $m^3 \cdot s^{-1}$. During the last two centuries, the Seine Estuary has been vastly altered by human activity [7]. As a result, the lower Seine River was changed from a dominantly natural system to an anthropogenically-controlled system [8]. Despite the highly dynamic nature of the system, tidal flats and salt marshes are still developed in the lower estuary; however, the intertidal surface area has drastically decreased during the last 30 years. The funnel-shaped estuary is exposed to the prevailing SSW winds, so that the intertidal regions at the mouth are subject to erosion under the combined effects of waves and currents [2]. The lower estuary is characterized by a distinct turbidity [7], which has a pronounced control on the sedimentation patterns on intertidal mudflats at the estuary mouth.

In the Seine Estuary, among others, monitoring of mudflat morphodynamics on different time scales has been developed for decades. The most basic method is the pole height manual measurement, which consists of putting a pole in the ground during a given period and regularly measuring (e.g., every day, week, or month) the bed level changes at the base of the pole. It represents a point-wise, low frequency method associated with a centimetric accuracy, which has been used to quantify accretion or erosion. Over the last 20 years, autonomous acoustic altimeters were developed to monitor high-resolution (sub-millimetric) and high-frequency (in the order of 1 Hz) bed elevation changes over long periods (years) [9,10]. However, the survey area is localized and measurements are not necessarily representative of the morphological changes of the entire mudflat, hence leading to large uncertainties when sediment budgets are evaluated. More recently, airborne LIDAR surveys

have been used to provide mudflat topography over large areas (on the order of 1 to 10 km^2). However, with vertical resolutions of decimetric order, infrequent survey return intervals, and their high deployment cost, airborne LiDAR surveys only allow us to capture long-term morphological changes. Terrestrial Laser Scanning (TLS) is a possible alternative [11,12], even though the ground coverage is spatially limited around the TLS and the presence of surficial residual water is a major constraint preventing backscattering of the emitted light, thus potentially masking large areas in TLS surveys. As a consequence, there is a methodological gap for monitoring fast and moderate spatial mudflat morphodynamic evolution that could be bridged by photogrammetric surveys from Unmanned Aerial Vehicles (UAVs).

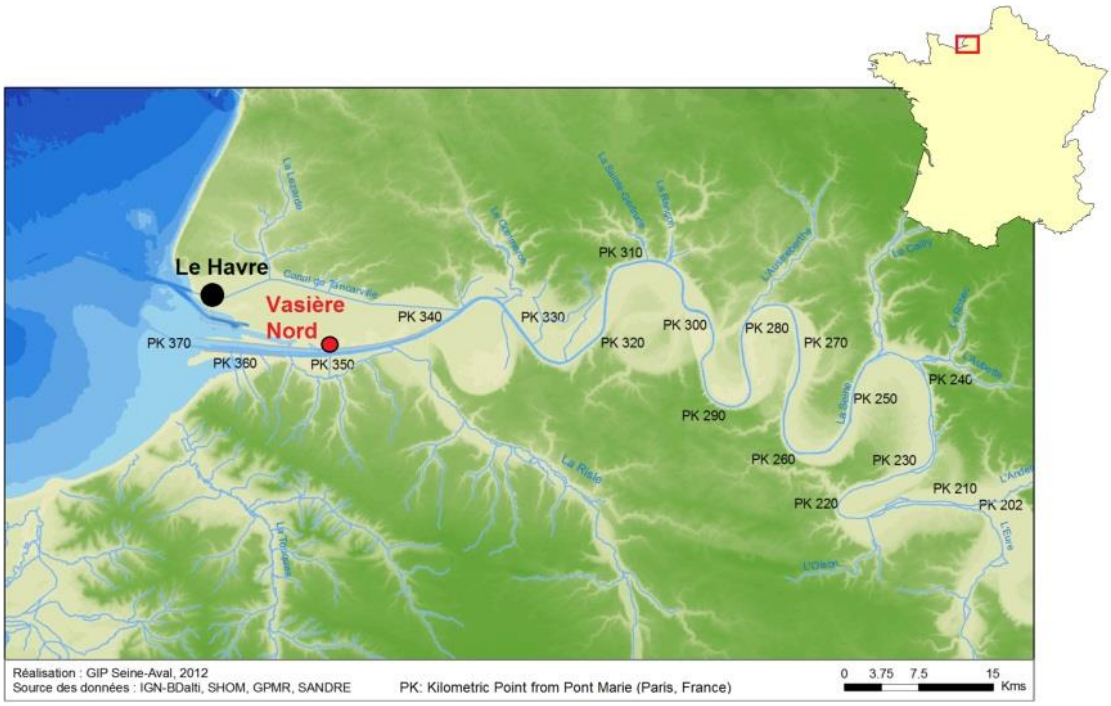

Figure 1. Study area in the Seine Estuary. This study focuses on the Vasière Nord area.

In a broader context, as mentioned in recent reviews on the subject [13,14], remote-sensing approaches using UAVs have been applied in a variety of research and operational domains, such as geomatics, navigation, surveying, engineering, robotics, and data processing. A wide range of platforms are now available, offering varying possibilities in terms of payload and flight-time autonomy. Thanks to the miniaturization of sensors and onboard electronics for data logging and control systems, a growing number of sensor types (e.g., optical camera, LiDAR, hyperspectral camera) can operate from a UAV, offering extensive possibilities to fully exploit the entire electromagnetic spectrum for remote sensing purposes [14]. Photogrammetric surveys from UAVs are particularly useful for environmental monitoring, in mountainous [15], agricultural [16], riverine, and coastal contexts [17–19]. Drones can provide surveys at higher temporal frequencies than airborne photogrammetry or airborne topographic LIDAR systems. They are also more flexible to use and more maneuverable. As they are not subject to the same regulations, they can be flown at low altitude, which is crucial in order to improve the resolution and accuracy of the data. With the recent developments in small UAVs and the use of Structure from Motion (SfM) algorithms, the rapid acquisition of topographic data at high spatial and temporal resolution is now possible at low cost [19–22]. The SfM approach is based on the SIFT (Scale-Invariant Feature Transform) image-to-image registration method [23,24]. In comparison with classic digital photogrammetry, the SfM workflow allows more automation and is therefore more straightforward for users [21,23].

UAV surveys have already been carried out above mudflat areas for imagery acquisitions [25–28], but rarely for photogrammetric purposes [29]. UAV photogrammetric surveys in mudflat areas are challenging. Mudflats are areas with difficult ground access, which is problematic for topographic surveys but also for deploying and surveying Ground Control Points (GCPs) for UAV surveys. Moreover, the duration of the time available for survey operations is controlled by low tide periods. Another difficulty is related to the stereo-photogrammetric method itself. Mudflats are generally characterized by surficial sediment with high water content, and even puddles and films of residual tidal water. In such environments, the stereo restitution method generally reaches its limits because of image correlation difficulties due to low textural pattern or sun-glint effects.

This study aims to demonstrate the potential and the limitations of high-resolution aerial photography and stereo restitution from a light UAV over mudflats. The results are interpreted in relation to the different morphological scales characterizing mudflat dynamics. Finally, these results are discussed in terms of the quality of the resulting imagery products, possible uses for mudflat monitoring, and future methodological improvements.

2. Study Area

This study is conducted within the Seine-Aval HYMOSED project (modeling of the HYdro-MOrpho-SEDimentary functioning of the Seine Estuary), with a focus on the "Vasière Nord" mudflat, the largest mudflat in the Seine Estuary (3.2 km^2), located in the northern part of the estuary mouth (Figure 1). The Seine river flow ranged from 100 $m^3 \cdot s^{-1}$ to 2000 $m^3 \cdot s^{-1}$ over the last 20 years, with a mean annual discharge around 500 $m^3 \cdot s^{-1}$. Previous studies show that deposition occurs in bursts during periods of low fluvial discharge, and is closely related to the highest spring tides and the presence of the turbidity maximum zone in the estuary mouth [2]. These deposits are dominated by fine sediments (<50 μm), which represent 70%–90% of the material. As in the upstream fluvial mudflat, erosion events of several centimeters are observed, mostly following deposition periods [30].

During the time frame of the study, three ALTUS altimeters [9] were deployed on the Vasière Nord mudflat along a transect perpendicular to the main channel. The ALTUS provided bed elevation measurements with sub-millimetric resolution and a sampling frequency of one measurement every four minutes between April 2014 and October 2015. The three ALTUS are located along a single transect, one near the vegetation on the top of the tidal flat, one in the central ("flat") portion, and one on or near the slope break. This distribution is to capture distinct processes, because the portions of the tidal flat may behave differently, both globally (*i.e.*, on a seasonal scale: erosion/deposition depending on flow strength at different moments of the tidal cycle, so with different depth of the overlying water-column) and at short time scales (because their immersion time differs in relation to tidal amplitude).

3. Materials and Methods

3.1. Data Processing Method

The procedure for deriving orthophotographs and DEMs is based on the SfM workflow for Multiview Stereophotogrammetry. The SfM algorithm implemented by PhotoScan® for the 3D surface reconstruction is divided into four main steps [22,31]:

i) Camera alignment by bundle adjustment. Common tie points are detected and matched on overlapping photographs so as to compute the external camera parameters (position and orientation) for each picture and refine the camera calibration parameters.
ii) From the estimated camera positions and the pictures themselves, stereophotogrammetric equations allow the software to compute the position of each tie point, so as to build a dense point cloud.

iii) A 3D polygonal mesh is then constructed as a representation of the object surface based on the dense point cloud.
iv) The reconstructed mesh can be textured and used to generate an orthophotograph. The DEM is computed by interpolating the irregular polygonal mesh onto a regular grid.

An orthophotograph is a mosaic of aerial photographs geometrically corrected for lens distortion and ground relief effects. Orthophotographs have the same scale throughout and can be used as maps. A DEM refers generically to a grid-based representation of topography built by the interpolation of topographic points on a regular grid. To be more specific, a Digital Surface Model (DSM) represents the elevations of the ground and all features on it (e.g., buildings, vegetation), while a Digital Terrain Model (DTM) is a bare ground representation [32]. This study is focused on DSMs, as directly computed by PhotoScan®. Nevertheless, it can be noticed that DSM and DTM are synonymous in the main part of the study area. In the following text, the terms DSM and DEM will be used interchangeably.

After construction, the DEM and orthophotograph are exported into a reference coordinates system (here, RGF93—Lambert 93).

DEM differencing consists of subtracting two diachronic DEMs in order to compute a DEM of Difference (DoD), *i.e.*, a grid of change in elevation that occurred between the two acquisition dates. In our case, the DSMs are subtracted using ESRI ArcGIS® software.

3.2. Technical Specifications of UAV Acquisition

The survey is performed by a DS6 hexacopter platform, provided by DroneSys, called DRELIO (Figure 2a). This electric multi-rotor UAV has a diameter of 0.8 m and is equipped with a collapsible frame allowing the UAV to be folded back for easy transportation. The DS6 weighs less than 4 kg and can handle a payload of 1.6 kg. To ensure a soft landing in case of technical problems, it is equipped with a parachute rescue system. Although DRELIO is able to perform an autonomous flight, take-off, and landing, ground station software is used to control the UAV during the flight.

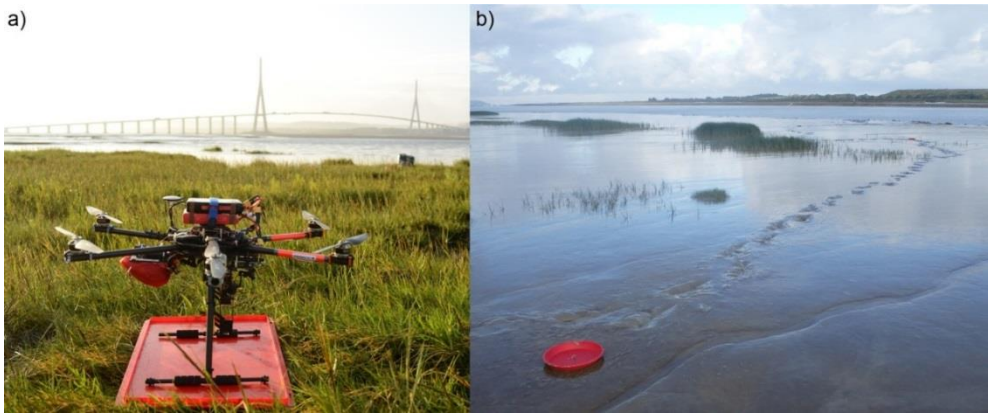

Figure 2. (**a**) The DRELIO UAV before take-off; (**b**) example of red target used as GCP.

To avoid sun glint effects at the water-saturated sediment surface, including on puddles and films of residual tidal water, flights were preferentially carried out in cloudy weather, and either early in the morning or late in the evening, if compatible with low tides. The flight autonomy of DRELIO 10 is about 20 min. It is equipped for nadir photography with a Nikon D700 digital reflex camera with a fixed focal length of 35 mm, taking one 12 Mpix photo in intervalometer mode every second. The onboard flight control system is composed of a GPS and an autopilot. The flight control is run by DJI® iOSD® software. The range of operation can extend up to 1 km. The typical velocity of the UAV is 3 $m \cdot s^{-1}$ in order to guarantee at least a 60% overlap between successive images (Figure 3) at an

altitude of 100 m. After the flight, the collected images are transferred from the camera to a computer in order to be processed.

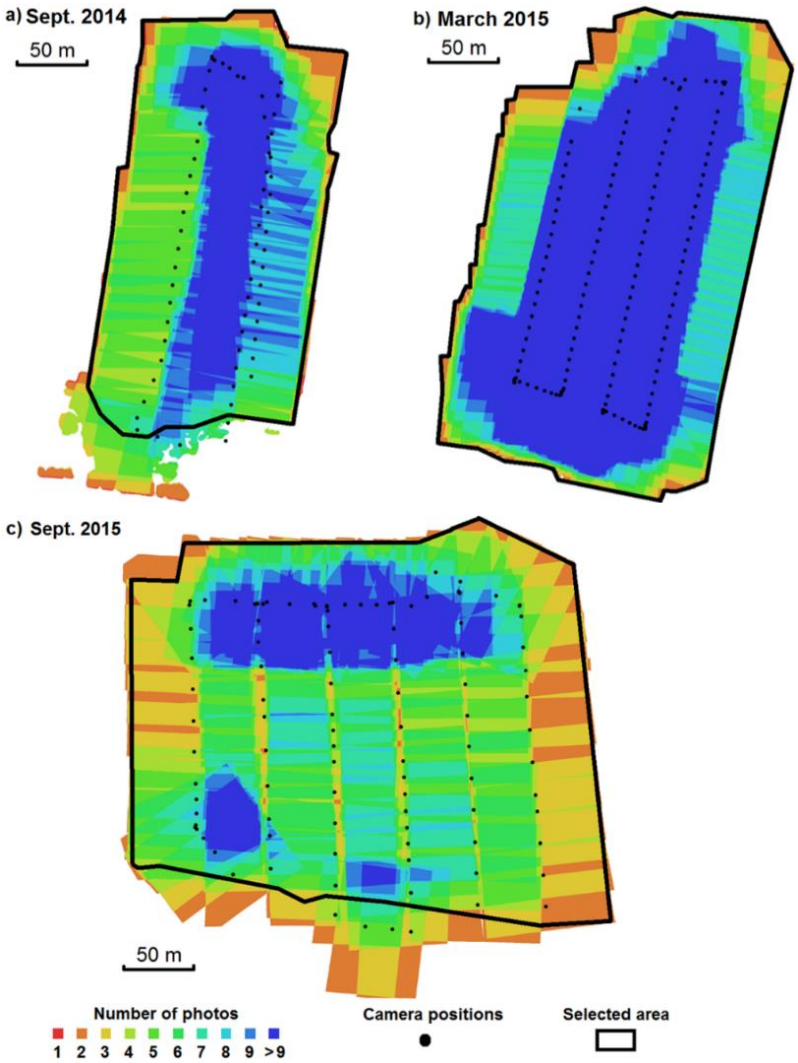

Figure 3. Overlapping images and computed camera positions for the three surveys: (**a**) September 2014, (**b**) March 2015 and (**c**) September 2015.

The payload limit does not permit the drone to be equipped with precise navigation and positioning equipment. As a result, Ground Control Points (GCPs) are required in order to register the results into a reference coordinates system (here, RGF93 Lambert 93 which is the official reference system in France). The GCPs consist of highly visible targets distributed over the survey area (Figure 2b). These targets are red discs 30 cm in diameter. They are georeferenced by a differential post-processed GPS, using a Topcon HiPer II GNSS receiver. The mean accuracy of the differential GPS (DGPS) survey is 3 cm horizontally and 4 cm vertically. Placing the GCPs and measuring their position is a very time-consuming step of the survey, particularly in mudflat areas where access by foot is challenging and sometimes restricted by impassable channels (for instance, the time window for setting up, measuring with DGPS and picking up the 23 targets for the survey on September 2015 was about 2 h). For time-efficiency purposes given the constraint of the tide, the targets were preferably laid out around the ALTUS sites (Figure 4a) in order to guarantee high accuracy in the main area of interest. The GCPs are imported in AgiSoft® PhotoScan Professional (version 1.1.5) to compute georeferenced orthophotos and DSMs.

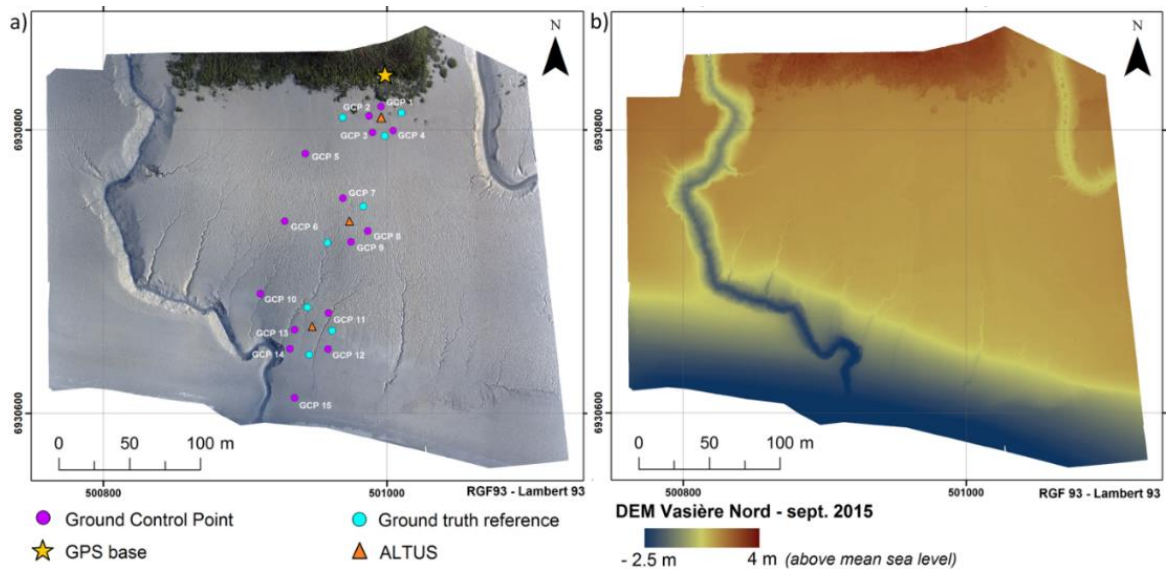

Figure 4. (**a**) Orthophotograph and (**b**) DEM resulting from the survey in September 2015.

3.3. Field Survey Data Collection

For this study, three surveys were carried out: the first one on 12 September 2014 (low river discharge), the second one on 11 March 2015 (one month after the peak flood period), and the last one on 2 September 2015 (back to low river discharge conditions). Table 1 summarizes the key parameters of each survey. The flights were operated at an altitude of around 100 m to achieve the best compromise between spatial resolution and ground coverage. Hence, this configuration provides a spatial resolution of about 2 cm/pixel and one flight is sufficient to cover the whole study area. Each photo covers an area of approximately 67 m $\times$ 45 m on the ground. Flight altitude impacts the ground coverage and spatial resolution of the images; however, the accuracy of the results is also limited by the accuracy of the differential GPS when measuring GCPs. Furthermore, flying at lower altitudes would yield a better resolution but reduced ground coverage. Given our intervelometer setup, a reduction in ground coverage would reduce image overlap, a step that is necessary in the stereo restitution process.

Table 1. Key parameters of the UAV surveys. The camera is a Nikon D700 with a fixed focal length of 35 mm.

	September 2014	**March 2015**	**September 2015**
Mean flying altitude	95.7 m	95.8 m	103.3 m
Nb. of acquired photos	316	168	247
Nb. of selected photos for processing	67	150	99
Nb. of GCP	12	15	15
Nb. of GR	7	8	8

As an example, during the survey carried out in September 2015, 250 photos were collected during the flight. Among these photos, 99 were selected for stereo restitution processing (Figure 3). We removed the photographs acquired during take-off and landing, the blurred photographs, and those duplicating other images. Before the UAV flight, 23 red targets were placed and measured by DGPS (Figure 4); 15 of them were used as GCPs and eight of them were used as a Ground Reference (GR) to assess the quality of the computed DSM and orthophoto.

4. Results

4.1. Orthophotograph and Digital Elevation Model

For each survey, an orthophotograph and a DEM are computed by SfM photogrammetry, providing a surface representation of the study area (example for September 2015 in Figure 4). The quality of the results is summarized in Table 2. The horizontal and vertical accuracy are mainly determined by the accuracy of the DGPS positioning of the GCPs. Accuracy is assessed using the set of GR targets (depicted by blue dots in Figure 4). The horizontal and vertical Root Mean Square Errors (RMSE) for each survey are summarized in Table 2. These errors are of the same order of magnitude as the uncertainty in the DGPS measurements.

Table 2. Quality of the results of the UAV surveys.

	September 2014	**March 2015**	**September 2015**
Point cloud density	550.5 pts/m^2	565.2 pts/m^2	495.8 pts/m^2
Orthophoto resolution	2.1 cm/pix	2.1 cm/pix	2.2 cm/pix
DEM resolution	4.2 cm/pix	4.2 cm/pix	4.5 cm/pix
Horiz./Vert. RMSE	2.5 cm/3.9 cm	1.5 cm/2.7 cm	1.6 cm/3.5 cm

Considering the flight configuration (nadir-pointing camera, parallel flight lines, constant flying height), the derived DEMs are likely to show broad-scale deformations [21,33]. These artefacts are reduced by including the GCP in the bundle adjustment step of the SfM workflow [31]. Nevertheless, as the GCPs are concentrated in the central part of the area, systematic errors likely remain on the eastern and western parts, where there is no GCP.

4.2. Surveying the General Trend of Evolution of the Area: DoDs and Volume Budgets

Repeated acquisitions of high-resolution DEMs enable mapping and monitoring of erosion and deposition, computing volumetric changes through time, and assessing sediment budgets [34,35]. Subtracting the earlier DEM from the later DEM, the DoDs produced here represent erosion as negative values and accretion as positive values.

The DEM of September 2014 is subtracted from the DEM of March 2015, and the DEM of March 2015 is subtracted from the DEM of September 2015. The resulting DoDs (Figure 5) provide a spatial representation of the general trend of morphological evolution of the area. The tidal creek situated on the western part of the study area appears to be highly mobile due to meandering rearrangement. The time step between the two surveys does not allow us to determine whether the timescale of this rearrangement is several months or a tidal cycle. The DoD between March 2015 and September 2015 also shows that the tidal creek in the northern part of the area is silting up.

To take into account the influence of DEM uncertainties on DoDs, we adopt the common procedure of specifying a Level of Detection threshold (LoD) [36,37]. The individual errors in the DEM are propagated into the DoD as:

$$\delta u_{DoD} = \sqrt{(\delta z_{MNT\,1})^2 + (\delta z_{MNT\,2})^2} \quad (1)$$

where δu_{DoD} is the propagated uncertainty in the DoD and $\delta z_{MNT\,1}$ and $\delta z_{MNT\,2}$ are the individual errors in DEMs used for the calculation of the DoD [34]. For this study, the LoD is calculated using the RMSE in each DEM. According to Equation (1), the uncertainties in the DoDs between September 2014 and March 2015 and between March 2015 and September 2015 are, respectively, $\delta u_{DoD_{sept2014–mar2015}} = 4.7$ cm and $\delta u_{DoD_{mar2015–sept2015}} = 4.4$ cm.

While imagery products are indeed exploitable at the required resolution level, the DoD shows artifacts (appearing particularly in the western part of both DoDs in Figure 5 and in the upper right-hand corner of the DoD between March 2015 and September 2015). These artifacts confirm

that the RMSEs of the DEMs are higher on the external parts of the study area, probably because of unsatisfactory auto-calibration during the bundle-adjustment step.

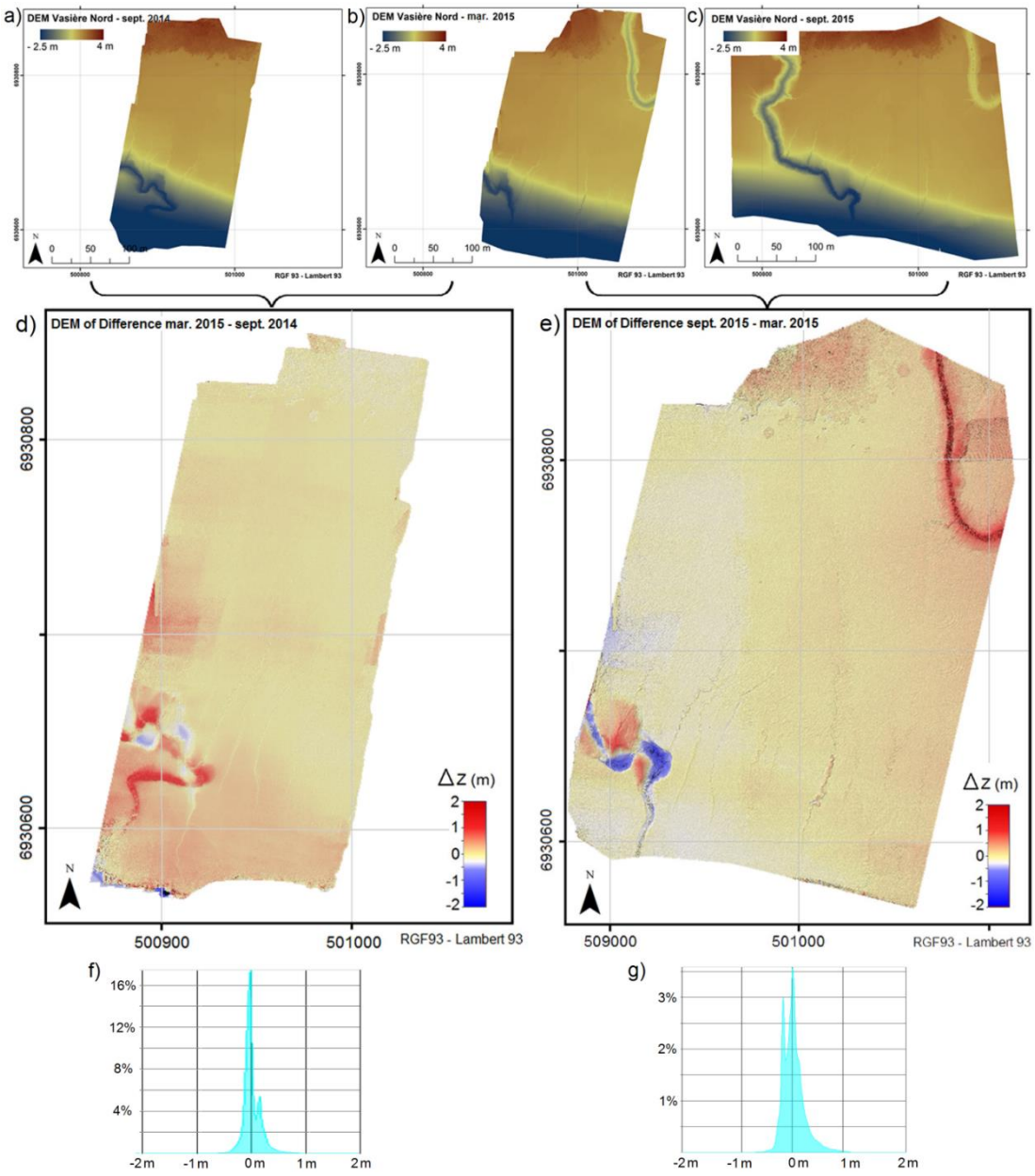

Figure 5. From the photogrammetric DEMs obtained in: (**a**) September 2014; (**b**) March 2015; and (**c**) September 2015, DEMs of Difference (DoD) (**d**,**e**) are computed. ΔZ is the vertical difference. Negative values (in blue) depict erosion and positive values (in red) depict accretion. Graphs (**f**,**g**) are the corresponding histograms of the amount of change.

For illustration purposes, a quantitative material balance at the scale of the study site is calculated on a reference area common to all surveys (Figure 6). A cross-shore strip was defined and the eroded or accreted volumes were calculated from the DoD between September 2014 and March 2015 and between March 2015 and September 2015. The results are presented in Table 3. Despite the high levels of uncertainty, these results show a general trend: deposition between September 2014 and March 2015 and scouring between March 2015 and September 2015.

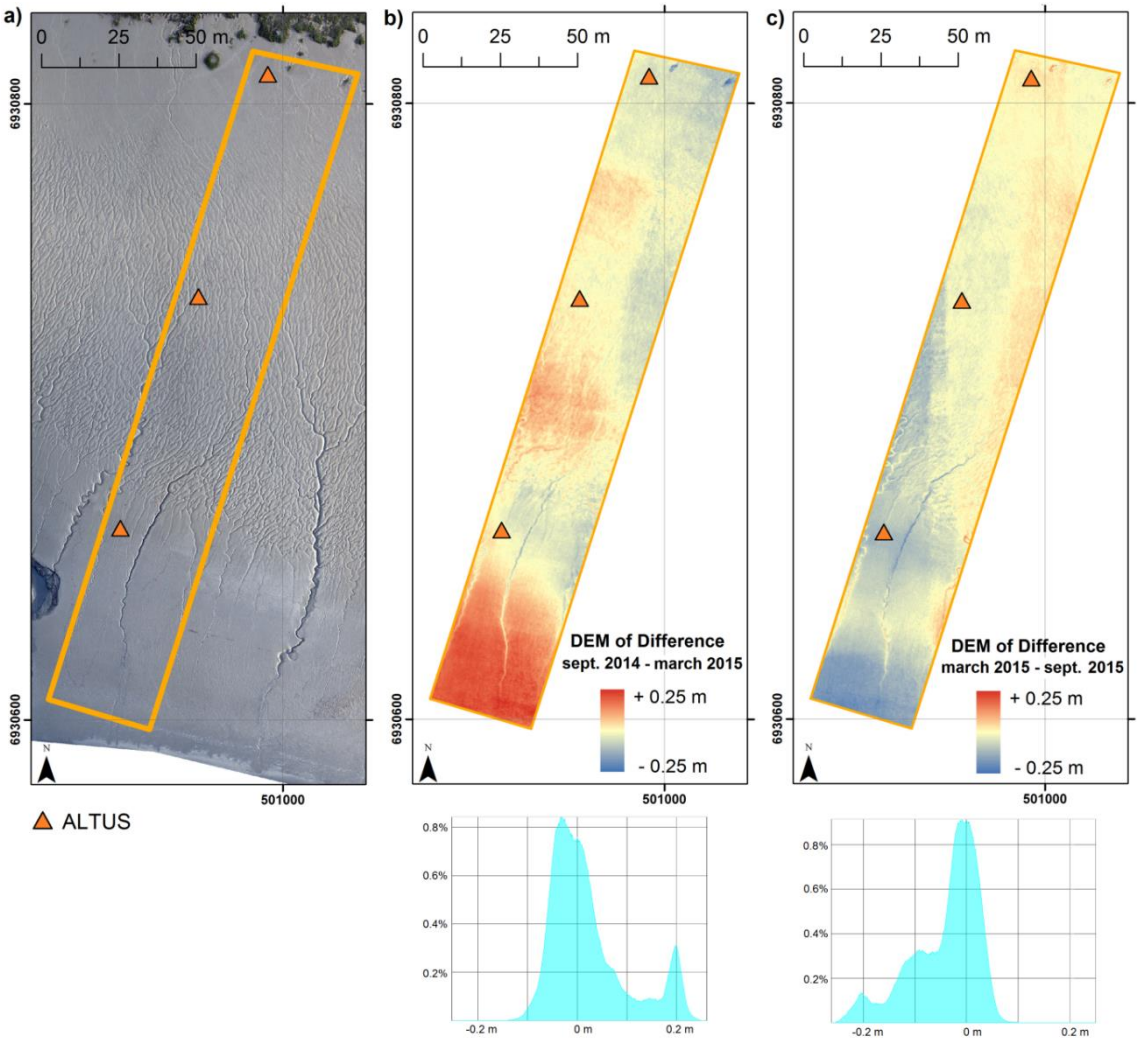

Figure 6. (**a**) Definition of a cross-shore strip for site-scale material balance calculations; (**b**) extract from the DoD between September 2014 and March 2015 and the corresponding histogram of amount of change; (**c**) extract from the DoD between March 2015 and September 2015 and the corresponding histogram of amount of change.

Table 3. Material balance over a cross-shore strip. The volume normalized with respect to the surface is given in brackets.

September 2014 to March 2015
Positive volume: +309.64 m^3 over a surface of 3961.57 m^2 ($\pm$186.19 m^3) normalized to +7.8 cm Negative volume: $-$130.82 m^3 over a surface of 3688.53 m^2 ($\pm$173.36 m^3) normalized to $-$3.5 cm
March 2015 to September 2015
Positive volume: +54.12 m^3 over a surface of 2444.29 m^2 ($\pm$107.55 m^3) normalized to +2.2 cm Negative volume: $-$360.74 m^3 over a surface of 5203.86 m^2 ($\pm$228.97 m^3) normalized to $-$6.9 cm

Very high accuracy is essential so that the "noise," the magnitude of the propagated error during DEM differencing [35,38], does not exceed the "signal," the magnitude of the vertical changes between diachronic acquisitions. As mentioned in [39], because of the coarse temporal resolution, the date of each survey sets bounds for the period during which changes occur but does not specify the precise timing or the agents of change.

4.3. Spatially-Extended Versus Point-Wise Altimetry: Comparing with ALTUS Measurements

As mentioned in Section 2, the ALTUS altimeters provide point-wise bed elevation measurements with a sub-millimetric resolution and a sampling frequency of one measurement every 4 min. Three ALTUS are located along a transect from the top of the tidal flat to the slope break. The spatial extent of the altimetry information offers new possibilities for the study of mudflat dynamics. The aim of this section is to illustrate the comparison between point-wise ALTUS measurements and spatialized data. For example, we compared the Δz variations in bed elevation measured by the ALTUS located in the north of the study area with the variations obtained from the stereo restitution DoDs.

For the period of study, the ALTUS measured an erosion of 2.3 cm between September 2014 and March 2015 and an accretion of 6.0 cm between March 2015 and September 2015. Rings with respective radii of 2 m, 5 m, and 10 m are extracted from the DoDs (Figure 7). As the ALTUS is visible on the aerial photos, it was reconstructed in the DEM and would have affected the comparison; therefore, a disc of radius 1 m was excluded from analysis (hence the choice of the ring for the reference surface). The average variations of altitude Δz over the reference surface are computed for each DoD. The results of the comparison are presented in Table 4.

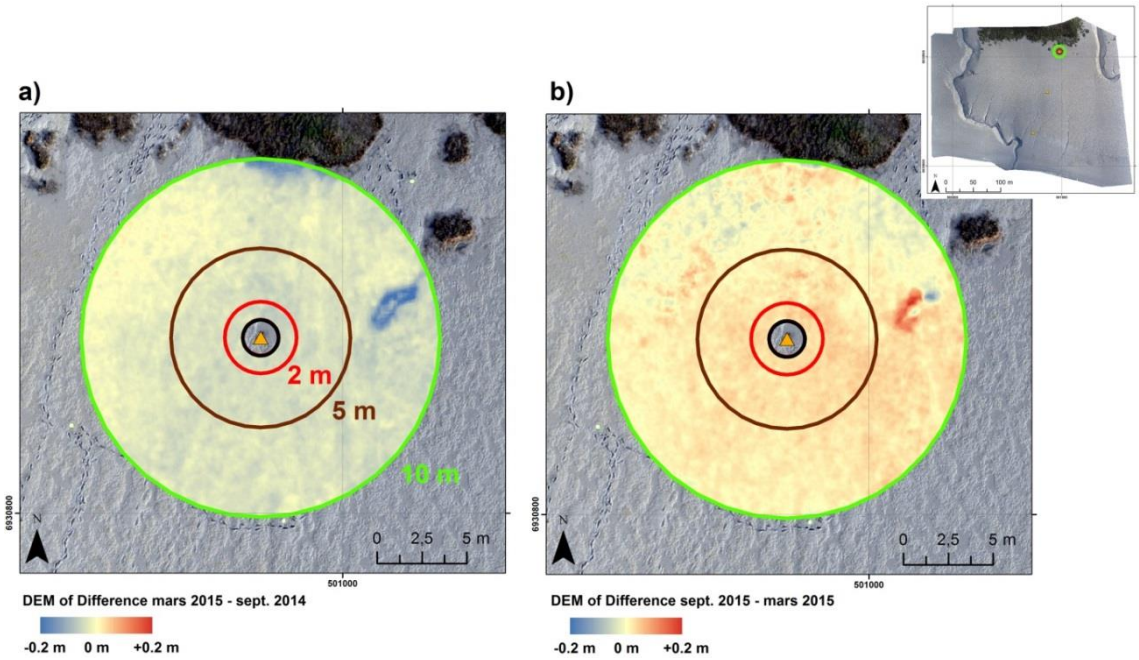

Figure 7. Rings centered on the ALTUS in the north of the study area (see the inlet) with external radii of 2 m, 5 m, and 10 m extracted from the DoD (**a**) between September 2014 and March 2015 and (**b**) between March 2015 and September 2015 (the internal radius of 1 m is meant to exclude the frame of the ALTUS, which masks the sediment interface on the imagery products).

Table 4. Evaluation of bed elevation changes obtained from stereo restitution DoDs around an ALTUS, compared with bed elevation change measured by this ALTUS.

	September 2014 to March 2015	March 2015 to September 2015
Δz variation measured by the ALTUS	−2.3 cm	+6.0 cm
Δz variation on the ring of 2 m radius	−4.9 cm (±4.7 cm)	+3.1 cm (±4.4 cm)
Δz variation on the ring of 5 m radius	−4.2 cm (±4.7 cm)	+2.6 cm (±4.4 cm)
Δz variation on the ring of 10 m radius	−3.7 cm (±4.7 cm)	+1.6 cm (±4.4 cm)

The budgets obtained from stereo restitution DoDs appear lower than the LoD. Nevertheless, by averaging over rings of metric size, local "noise" (random error) is partly removed and the remaining error is mainly due to a coherent bias compared to the ALTUS measurement. In other words, the error is mainly due to accuracy rather than precision, and the relative magnitudes of the budgets are still exploitable.

Both the ALTUS and DoDs budgets show a seasonal tendency, with erosion between September 2014 and March 2015 and deposit between March 2015 and September 2015. Despite the possible bias on DoDs budgets, the stereo restitution DoDs seem to overestimate the decrease in bed elevation during the winter period and underestimate the increase in bed elevation during the summer period, as compared to the ALTUS measurements. That suggests the ALTUS may act as a sediment trap. The evolution of the average altitude variation when changing the reference surface (the ring size) is due to the spatial variability in the considered zone (texture, mean slope, vegetation patches, *etc.*). The same comparative test in other areas would likely yield more significant differences as the ring size increases due to spatial variability, induced for instance by the presence of a slope break or tidal creeks. The difference between the ALTUS measurement and stereo restitution DoD also arises from this spatial variability, which cannot be taken into account by the ALTUS, as well as from the uncertainty in the stereo restitution products (which is of the same order as the post-processed RTK GPS accuracy, *i.e.*, 3 cm horizontally and 4 cm vertically).

4.4. Surveying Tidal Creeks

As UAV stereophotogrammetry allows a multi-scale approach, typical sedimentary structures in the intertidal zone of the mudflat can be studied. As an example, the morphodynamics of the tidal-creek situated in the western part of the survey area can be described with sufficient resolution and accuracy so as to capture fine geomorphological variations (in the order of centimeters). Figure 8 depicts the meandering rearrangement between the successive orthophotographs and on the DoD. As before, material balance was computed for the two periods (Table 5). The rapid migration of the tidal creek mouth (connecting with a main channel) is remarkably captured, as well as the meandering pattern evolution.

High-resolution orthophotographs and DEMs also enable us to identify and map the morphology of micro-channels perpendicular to the main tidal creek (Figure 9a). From the repeated surveys, we can study the migration of these micro-creeks and their meandering dynamics (Figure 9b). The main geometric features of the micro-creek (length, width, depth, and main slope of the thalweg) can be extracted as shown on the longitudinal and transverse vertical profiles in Figure 9c,d. All of these parameters allow us to characterize the trapping or exfiltration capacity of the tidal creek networks. For example, we monitored the evolution of a micro-creek between the three surveys (Figure 9). On one hand, the upper section of the micro-creek (from A to C) located on the upper tidal flat did not move laterally at the annual scale, while on the other hand the lower part of the micro-creek located in the sloping portion of the mudflat, downstream of location C, significantly migrated, showing typical braided system morphodynamics. Overall, the upper tidal flat seems to be accreting and eroding on a seasonal scale (Sections 1 and 2 at location A) without lateral migration.

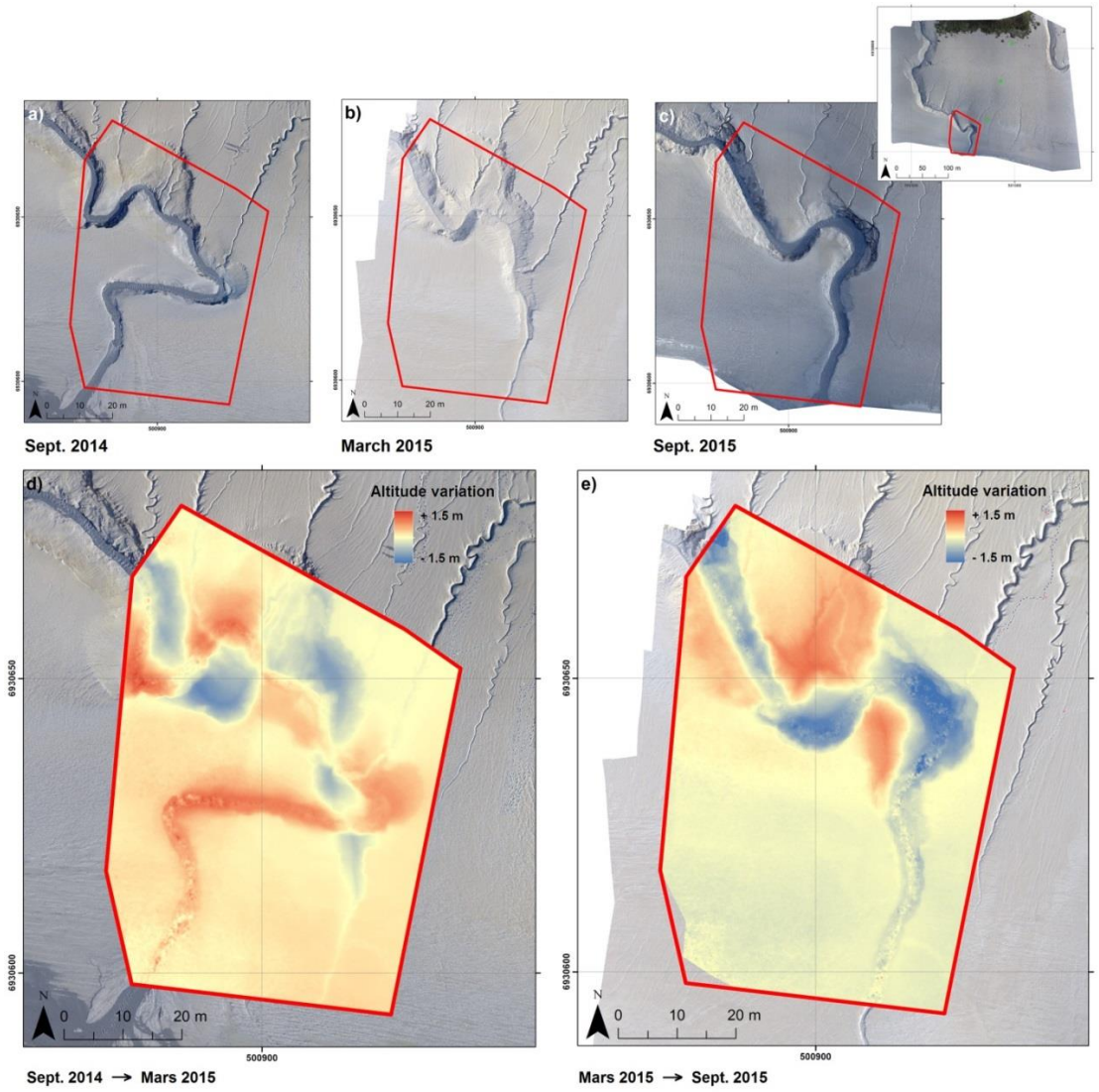

Figure 8. (**a**–**c**) Positioning of the studied portion of the tidal creek common to the successive orthophotographs. Extract of the DoD (**d**) between September 2014 and March 2015 and (**e**) between March 2015 and September 2015.

Table 5. Material balance on a portion of the western tidal creek. The volume normalized with respect to the considered surface is given in brackets.

September 2014 to March 2015
Total material balance: +425.18 m^3 ($\pm$180.74 m^3)
normalized to +11.0 cm
Positive volume: +686.73 m^3 over a surface of 2908.33 m^2 ($\pm$136.69 m^3)
normalized to + 23.6 cm
Negative volume: $-$261.55 m^3 over a surface of 937.26 m^2 ($\pm$44.05 m^3)
normalized to $-$27.9 cm
March 2015 to September 2015
Total material balance: $-$402.94 m^3 ($\pm$167.51 m^3)
normalized to $-$10.6 cm
Positive volume: +314.06 m^3 over a surface of 1058.47 m^2 ($\pm$46.57 m^3)
normalized to +29.7 cm
Negative volume: $-$717.00 m^3 over a surface of 2748.59 m^2 ($\pm$120.93 m^3)
normalized to $-$26.1 cm

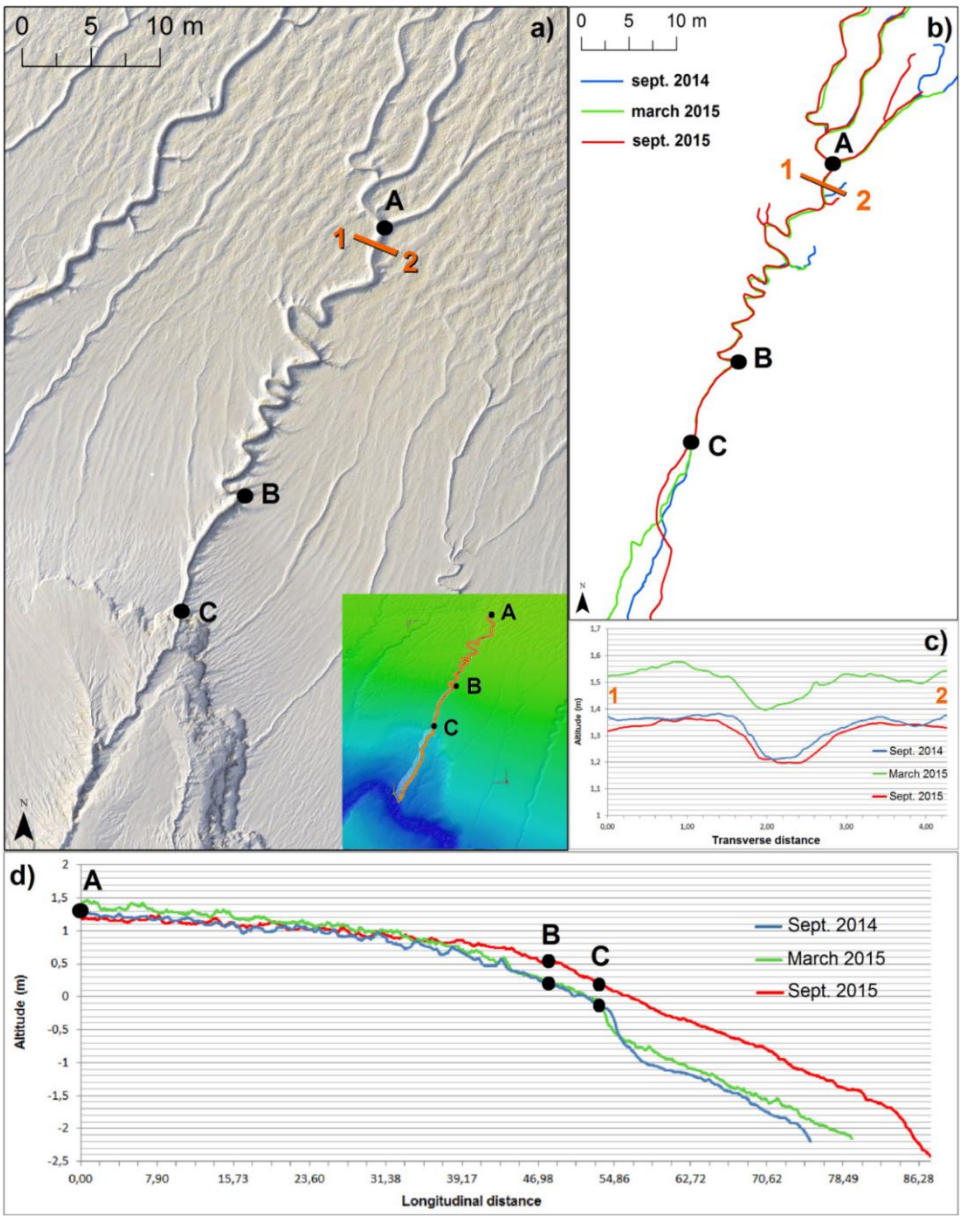

Figure 9. (**a**) Display of a micro-creek in the inter-tidal zone on an extract of the orthophoto of March 2015 (and in the inlet, the corresponding position on an extract of the DEM); (**b**) diachronic monitoring of the micro-creek position. The thalweg of the micro-creek is manually plotted from the orthophotographs using ArcGIS®software. (**c**) Example of a transverse profile showing the incision shape and the depth of the micro-creek; (**d**) example of a longitudinal profile.

4.5. Surveying Plant Ground Cover

Observing salt marsh vegetation patterns is an added capability of SfM from UAVs that can be explored by the scientific community studying mudflats. The evolution of ground-cover by plants can be assessed from the successive orthophotographs and DEMs. Figure 10 shows the DoD of the northern part of the study area. Ground cover by plants decreases between September 2014 and March 2015 (Figure 10a) and increases between March 2015 and September 2105 (Figure 10b). Comparing the September 2014 and September 2015 surveys (Figure 10c), so as to avoid the effect of the growth cycle of the plants by considering a timespan of a complete year, the elevation levels appear to be very similar (less than 5 cm difference), as expected. The altitude variations associated with vegetation are also visible in the stack of vertical profiles extracted from the successive DEMs (Figure 10d,e). The effect

of the vegetation on sediment hydrodynamics can also be studied from this UAV photogrammetry dataset. Here, the boundary of the vegetated area was eroded (by more than 20 cm) between September 2014 and March 2015, corresponding to a horizontal retreat of around 1 m of the vegetation cover.

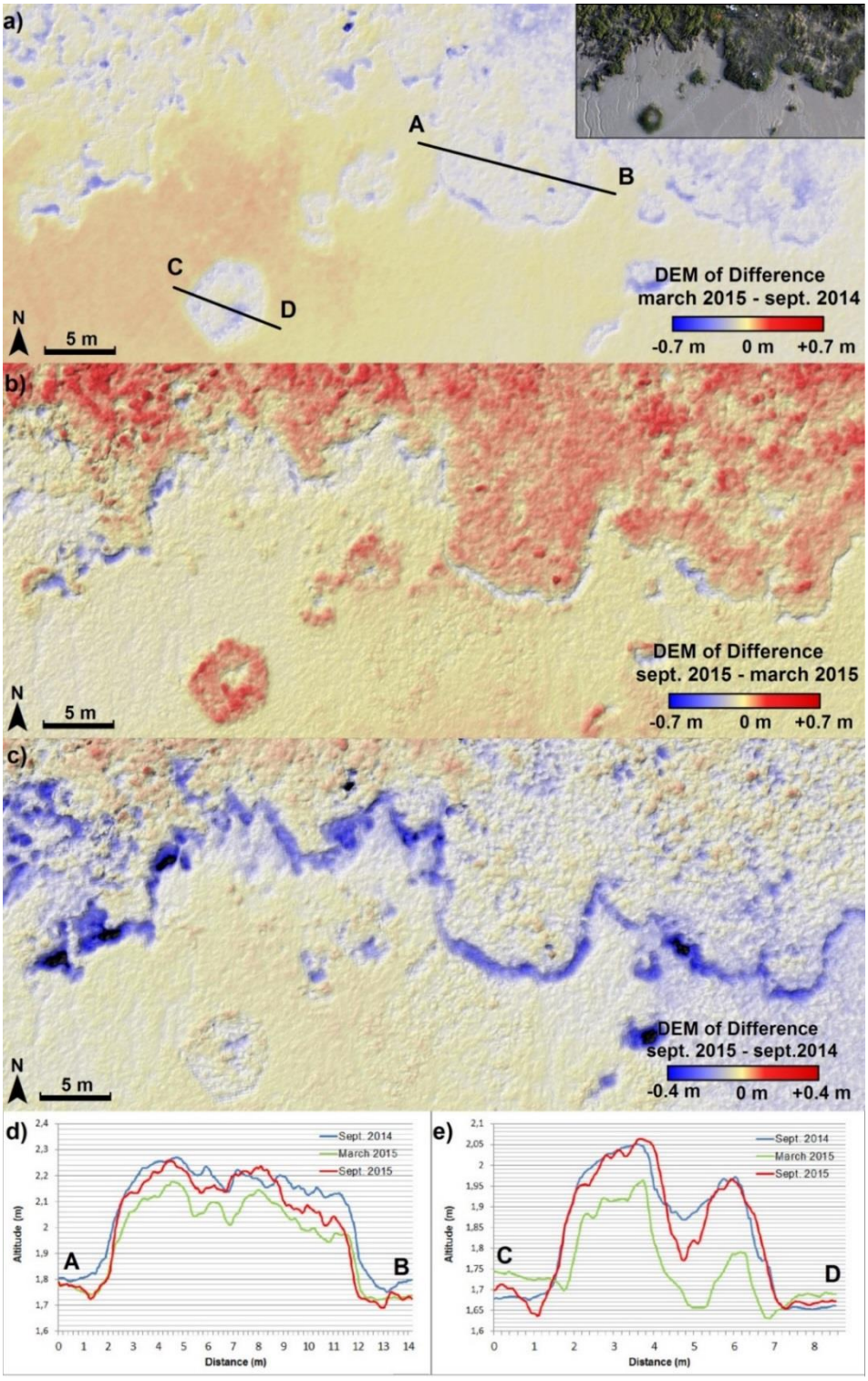

Figure 10. (**a**) Extract of the DoD between September 2015 and March 2015. The inlet shows the corresponding extract of the orthophoto. (**b**) Extract of the DoD between March 2015 and September 2014; (**c**) extract of the DoD between September 2015 and September 2014; (**d**,**e**) A–B and C–D vertical profiles extracted from the DEM (September 2014, March 2015, and September 2015).

The spatial resolution of satellite and high-altitude aerial data is not sufficient to capture such fine variations in the time evolution of the plant ground cover. Furthermore, flights at lower altitudes can be planned in order to achieve a better resolution that would allow classification of the different plant species, as was already done for precision agriculture [14,40,41]. For example, in this study, the flights were operated at an altitude of around 100 m with a 35 mm focal length, providing a spatial resolution of about 2 cm/pixel. Flying at 50 m altitude would increase the spatial resolution of the images to 1 cm/pixel. Since the ground coverage would be reduced, the flight speed would have to be reduced in order to maintain sufficient overlap between the images. Note that increasing the resolution does not necessarily increase the DEM accuracy, as it is mainly controlled by the DGPS accuracy, and in fact the present dataset already reaches the upper limit of accuracy.

5. Discussion

5.1. Limits for Applications of SfM from UAVs in Mudflat Environments

As previously mentioned, in mudflat areas, placing the GCPs and measuring their positions is a time-consuming step of the survey (about 2 h for setting up, measuring with the DGPS, and picking up the 23 targets on September 2015). This is a major concern in a context where the survey is restricted by the low-tide schedule. This results in few GCPs and ground truth references, with a sub-optimal spatial repartition. The sensitivity of the photogrammetric processing chain to the absence of GCPs in peripheral zones of the surveyed area appears to be particularly severe in this mudflat context. To assess the impact of the GCP distribution, a stereo restitution has been computed without using the GCP of the southern part (GCP 10 to 15 in Figure 4). In this case, the horizontal RMSE is 2.0 cm and the vertical RMSE is 5.4 cm, while the vertical error in the southern part increases to 10 cm. Decimetric or even metric resolution may be sufficient for a descriptive morphological study or rough volume monitoring. However, centimetric accuracy may be required in diachronic studies involving repeated acquisitions in order to limit systematic volumetric errors and thus to track low-amplitude morphological changes.

The SfM approach allows a higher level of automation [20,23], but systematic errors are expected to be more pronounced in the resulting DEMs [33]. According to [31], including GCPs in the bundle-adjustment enables us to reduce z-error. However, the repartition of the GCPs also appears to be a key factor affecting systematic errors. The presence of such uncertainties in the resulting DEM limits the potential of SfM for sediment budgeting to areas where the morphological variations are greater than the LoD. The calculation of the LoD is also made challenging by the small number of GRs. The RMSE is only computed on seven or eight GRs, which are located in the area of main interest (as are the GCPs). Furthermore, as the RMSE is averaged across the surface, this approach hypothesizes that the LoD is spatially homogeneous [37]. Spatially quantifying the accuracy of DEMs is difficult since it requires a higher accuracy validation surface as the ground-truth reference [38]. In our case, no synchronous reference data (Terrestrial Laser Scan—TLS—, aerial topographic LiDAR) are available.

In [20], it is also reported that another limitation of the SfM approach is the dependence on image texture, since the image-matching algorithm relies on it. The SfM restitution is therefore challenging over flat and uniform surfaces or highly reflective surfaces such as mudflats where the surface sediment is water-saturated. The presence of puddles and films of residual tidal water covering the mudflat amplifies the image correlation issue. However, in the present study, the stereo restitution process provides satisfying results despite the mudflat context. Indeed, high image resolution enables us to capture textural details (small channels, ripples, footprints, *etc.*), which contribute to the efficiency of the SfM photogrammetry process. Such details would not be visible on aerial or satellite imagery typically having lower resolution.

The high resolution and accuracy of the DEMs enable us to limit error propagation in DEM differencing. Certain references [35,37] propose methods for estimating the magnitude of DEM

uncertainty without ground truth comparison, using only the inherent parameters of the raw data. These methods (initially developed for TLS data) consider the DEM quality as a function of survey point quality, point density, topographic complexity and roughness of the area, and interpolation methods. Considering the high point density (about 500 points/m^2) and the relatively flat relief, the errors due to interpolation are expected to be low [38]. Thus, these methods of spatial assessment of the error are adapted to the raw TLS point cloud, but not necessarily for point clouds resulting from SfM workflow.

Compared to point-wise ALTUS altimeters, DoDs provide a spatial assessment of geomorphological variations. The resulting sediment budgets thus take into account the spatial variability of the mudflat. On the contrary, ALTUS altimeters provide continuous recordings of the altitude variations, while a DoD has a coarse temporal resolution since it represents the accumulation of the changes that occurred between the dates of each survey. The two approaches complement one another, providing insights on the dynamics of the estuary and the underlying processes.

5.2. Practical Guidelines for UAV Monitoring of Mudflats

Here we propose a number of guidelines that will help to optimize the quality of the acquired data for SfM from UAV over mudflats. To limit sun glint effects at the water-saturated sediment surface, including on puddles and films of residual tidal water, flights were preferentially carried out in cloudy weather, and either early in the morning or late in the evening, if compatible with low tides. When possible, changing the orientation of the camera may also help improve the efficiency of the SfM workflow [33].

The flight altitude of the UAV has to be low enough that the acquired photographs have a sufficiently fine resolution to capture textural details contributing to the smooth running of the SfM workflow.

Results show that the accuracy of the DEM would be greater if GCPs were more evenly distributed over the entire survey area, including the peripheral zones. Hence, a compromise has to be found between acquisition time and target distribution. Some targets could be easily added at the limit of the vegetated zone. Moreover, it may be difficult for people who set up the targets to have a synoptic view of their repartition. The positions of the targets (used as GCPs and GRs) could be chosen beforehand, taking into account the terrain difficulties, and people could go out in the field with a hand-held GPS to set up the targets at the selected positions. An alternative solution is to change the survey strategy, particularly the flight plan, following the guidelines proposed by [33] in order to mitigate surface deformation. A foreseeable improvement, thanks to sensor miniaturization, would be to reduce the number of required targets by making use of sufficiently accurate onboard navigation sensors.

6. Conclusions

UAV photographs and the resulting DEM, orthophotographs, and DoD provide copious information for mudflat studies. Given the ground texture of such environments, the stereo restitution process is made possible thanks to the high spatial resolution of the UAV photographs. For each UAV mission, computed orthophotographs and DEMs with about 2 cm and 4 cm of resolution, respectively, have been realized. The horizontal and vertical RMSEs of the DEM, computed on eight GR points, are less than 5 cm.

Providing a synoptic view, aerial photogrammetric surveys add significant value when monitoring large areas. The spatial extent of the information is a key asset in the study of mudflat dynamics. Both long-shore and cross-shore variability are captured with high resolution and accuracy. UAV photogrammetry also enables multiscale studies by characterizing and quantifying sedimentation dynamics to monitor both the general trend over large areas as well as the evolution of smaller structures, hence possibly inferring the role of the smaller structures on the larger-scale response.

In order to circumvent the effects of temporal interpolation of rates of change, this diachronic approach could be enriched by combining it with the pointwise, time-continuous ALTUS dataset in order to infer when and why the changes occur.

Acknowledgments: This study has been carried out in the framework of the HYMOSED project funded by the Seine-Aval 5 research program. This work has been also supported by the EU through the FP7 project IQmulus (FP7-ICT-2011-318787).

Author Contributions: Marion Jaud performed data processing and analysis and wrote the manuscript. Florent Grasso and Romaric Verney contributed to data analysis and to the writing of Sections 1 and 2. Nicolas Le Dantec contributed to data analysis and supervised the writing of the manuscript. Christophe Delacourt developed the research plan for the UAV survey and provided guidance on the overall project. Jérôme Ammann organized field data collection and pre-processed the UAV and GPS data. Julien Deloffre collected the ALTUS data, while Philippe Grandjean collected the UAV data.

Conflicts of Interest: The authors declare no conflict of interest.

References

1. Deloffre, J.; Lafite, R.; Lesueur, P.; Lesourd, S.; Verney, R.; Guézennec, L. Sedimentary processes on an intertidal mudflat in the upper macrotidal Seine estuary, France. *Estuar. Coast. Shelf Sci.* **2005**, *64*, 710–720. [CrossRef]
2. Deloffre, J.; Verney, R.; Lafite, R.; Lesueur, P.; Lesourd, S.; Cundy, A.B. Sedimentation on intertidal mudflats in the lower part of macrotidal estuaries: Sedimentation rhythms and their preservation. *Mar. Geol.* **2007**, *241*, 19–32. [CrossRef]
3. Neumeier, U. Velocity and turbulence variations at the edge of saltmarshes. *Cont. Shelf Res.* **2007**, *27*, 1046–1059. [CrossRef]
4. Neumeier, U.; Ciavola, P. Flow resistance and associated sedimentary processes in a spartina maritima salt-marsh. *J. Coast. Res.* **2004**, *20*, 435–447. [CrossRef]
5. Ganthy, F.; Sottolichio, A.; Verney, R. Seasonal modification of tidal flat sediment dynamics by seagrass meadows of Zostera noltii (Bassin d'Arcachon, France). *J. Mar. Syst.* **2013**, *109*, S233–S240. [CrossRef]
6. O'Brien, D.J.; Whitehouse, R.J.S.; Cramps, A. The cyclic development of a macrotidal mudflat on varying timescales. *Cont. Shelf Res.* **2014**, *20*, 1593–1619. [CrossRef]
7. Avoine, J.; Allen, G.P.; Nichols, M.; Salomon, J.C.; Larsonneur, C. Suspended sediment transport in the Seine estuary, France—Effect of man-made modifications on estuary-shelf sedimentology. *Mar. Geolol.* **1981**, *40*, 119–137. [CrossRef]
8. Lesourd, S.; Lesueur, P.; Brun-Cottan, J.-C.; Auffret, J.-P.; Poupinet, N.; Laignel, B. Morphosedimentary evolution of the macrotidal Seine estuary subjected to human impact. *Estuaries* **2001**, *24*, 940–949. [CrossRef]
9. Bassoullet, P.; Le Hir, P.; Gouleau, D.; Robert, S. Sediment transport over an intertidal mudflat: Field investigations and estimation of fluxes within the "Baie de Marennes-Oleron" (France). *Cont. Shelf Res.* **2000**, *20*, 1635–1653. [CrossRef]
10. Andersen, T.J.; Pejrup, M.; Nielsen, A.A. Long-term and high resolution measurements of bed level changes in a temperate, microtidal coastal lagoon. *Mar. Geol.* **2006**, *226*, 115–125. [CrossRef]
11. Anthony, E.J.; Dolique, F.; Gardel, A.; Gratiot, N.; Proisy, C.; Polidori, L. Nearshore intertidal topography and topographic-forcing mechanisms of an Amazon-derived mud bank in French Guiana. *Cont. Shelf Res.* **2008**, *28*, 813–822. [CrossRef]
12. Brasington, J.; Vericat, D.; Rychkov, I. Modeling river bed morphology, roughness, and surface sedimentology using high resolution terrestrial laser scanning. *Water Resour. Res.* **2012**, *48*. [CrossRef]
13. Colomina, I.; Molina, P. Unmanned aerial systems for photogrammetry and remote sensing: A review. *ISPRS J. Photogramm. Remote Sens.* **2014**, *92*, 79–97. [CrossRef]
14. Pajares, G. Overview and Current Status of Remote Sensing Applications Based on Unmanned Aerial Vehicles (UAVs). *Photogramm. Eng. Remote Sens.* **2015**, *81*, 281–329. [CrossRef]
15. Stumpf, A.; Malet, J.-P.; Kerle, N.; Niethammer, U.; Rothmund, S. Image-Based Mapping of Surface Fissures for the Investigation of Landslide Dynamics. *Geomorphology* **2013**, *186*, 12–27. [CrossRef]

16. Honkavaara, E.; Saari, H.; Kaivosoja, J.; Pölönen, I.; Hakala, T.; Litkey, P.; Mäkynen, J.; Pesonen, L. Processing and Assessment of Spectrometric, Stereoscopic Imagery Collected Using a Lightweight UAV Spectral Camera for Precision Agriculture. *Remote Sens.* **2013**, *5*, 5006–5039. [CrossRef]
17. Delacourt, C.; Allemand, P.; Jaud, M.; Grandjean, P.; Deschamps, A.; Ammann, J.; Cuq, V.; Suanez, S. DRELIO: An Unmanned Helicopter for Imaging Coastal Areas. *J. Coast. Res.* **2009**, *56*, 1489–1493.
18. Lejot, J.; Piegay, H.; Hunter, P.D.; Moulin, B.; Gagnage, M. Utilisation de la télédétection pour la caractérisation des corridors fluviaux: Exemples d'applications et enjeux actuels. *Géomorphol. Relief Process. Environ.* **2011**, *2*, 157–172. [CrossRef]
19. Mancini, F.; Dubbini, M.; Gattelli, M.; Stecchi, F.; Fabbri, S.; Gabbianelli, G. Using Unmanned Aerial Vehicles (UAV) for High-Resolution Reconstruction of Topography: The Structure from Motion Approach on Coastal Environments. *Remote Sensing* **2013**, *5*, 6880–6898. [CrossRef]
20. Fonstad, M.A.; Dietrich, J.T.; Courville, B.C.; Jensen, J.L.; Carbonneau, P.E. Topographic structure from motion: A new development in photogrammetric measurement. *Earth Surf. Process. Landf.* **2013**, *38*, 421–430. [CrossRef]
21. Westoby, M.J.; Brasington, J.; Glasser, N.F.; Hambrey, M.J.; Reynolds, J.M. "Structure-from-Motion" photogrammetry: A low-cost, effective tool for geoscience applications. *Geomorphology* **2012**, *179*, 300–314. [CrossRef]
22. Woodget, A.S.; Carbonneau, P.E.; Visser, F.; Maddock, I.P. Quantifying submerged fluvial topography using hyperspatial resolution UAS imagery and structure from motion photogrammetry. *Earth Surf. Process. Landf.* **2015**, *40*, 47–64. [CrossRef]
23. James, M.R.; Robson, S. Straightforward reconstruction of 3D surfaces and topography with a camera: Accuracy and geoscience application. *J. Geophys. Res.* **2012**, *117*. [CrossRef]
24. Lowe, D.G. Object recognition from local scale-invariant features. In Proceedings of the 7th IEEE International Conference on Computer Vision (ICCV), Kerkyra, Corfu, Greece, 20–25 September 1999; pp. 1150–1157.
25. Wan, H.; Wang, Q.; Jiang, D.; Fu, J.; Yang, Y.; Liu, X. Monitoring the Invasion of Spartina alterniflora Using Very High Resolution Unmanned Aerial Vehicle Imagery in Beihai, Guangxi (China). *Sci. World J.* **2014**, *2014*, 1–7.
26. Kelcey, J.; Lucieer, A. Sensor Correction of a 6-Band Multispectral Imaging Sensor for UAV Remote Sensing. *Remote Sens.* **2012**, *4*, 1462–1493. [CrossRef]
27. Cuvilliez, A.; Lafite, R.; Deloffre, J.; Lemoine, M.; Langlois, E.; Sakho, I. River flow control on intertidal mudflat sedimentation in the mouth of a macrotidal estuary. *Geomorphology* **2015**, *239*, 174–181. [CrossRef]
28. Van Prooijen, B.C.; Zhu, Q.; Brouwer, R.L.; He, Q. Horizontal coherent structures between tidal flat and channel. In Proceedings of the Coastal Sediments 2015, San Diego, CA, USA, 11–15 May 2015.
29. Ramirez-Juidias, E. Study of Erosion Processes in the Tinto Salt-Marshes with Remote Sensing Images. *Adv. Image Video Process.* **2014**, *2*, 39–52. [CrossRef]
30. Verney, R.; Deloffre, J.; Brun-Cottan, J.-C.; Lafite, R. The effect of wave-induced turbulence on intertidal mudflats: Impact of boat traffic and wind. *Cont. Shelf Res.* **2007**, *27*, 594–612. [CrossRef]
31. Javernick, L.; Brasington, J.; Caruso, B. Modeling the topography of shallow braided rivers using Structure-from-Motion photogrammetry. *Geomorphology* **2014**, *213*, 166–182. [CrossRef]
32. Maune, D.F. *Digital Elevation Model Technologies and Applications: The DEM Users Manual*, 2nd ed.; American Society for Photogrammetry and Remote Sensing: Bethesda, MD, USA, 2007.
33. James, M.R.; Robson, S. Mitigating systematic error in topographic models derived from UAV and ground-based image networks. *Earth Surf. Process. Landf.* **2014**, *39*, 1413–1420. [CrossRef]
34. Brasington, J.; Langham, J.; Rumsby, B. Methodological sensitivity of morphometric estimates of coarse fluvial sediment transport. *Geomorphology* **2003**, *53*, 299–316. [CrossRef]
35. Wheaton, J.M.; Brasington, J.; Darby, S.E.; Sear, D.A. Accounting for uncertainty in DEMs from repeat topographic surveys: Improved sediment budgets. *Earth Surf. Process. Landf.* **2009**, *35*, 136–156. [CrossRef]
36. Fuller, I.C.; Large, A.R.G.; Charlton, M.E.; Heritage, G.L.; Milan, D.J. Reach-scale sediment transfers: An evaluation of two morphological budgeting approaches. *Earth Surf. Process. Landf.* **2003**, *28*, 889–903. [CrossRef]
37. Milan, D.J.; Heritage, G.L.; Large, A.R.G.; Fuller, I.C. Filtering spatial error from DEMs: Implications for morphological change estimation. *Geomorphology* **2011**, *125*, 160–171. [CrossRef]

38. Heritage, G.L.; Milan, D.J.; Large, A.R.G.; Fuller, I.C. Influence of survey strategy and interpolation model on DEM quality. *Geomorphology* **2009**, *112*, 334–344. [CrossRef]
39. James, L.A.; Hodgson, M.E.; Ghoshal, S.; Latiolais, M.M. Geomorphic change detection using historic maps and DEM differencing: The temporal dimension of geospatial analysis. *Geomorphology* **2012**, *137*, 181–198. [CrossRef]
40. Blumenthal, D.; Booth, D.T.; Cox, S.E.; Ferrier, C.E. Large-scale Aerial Images Capture Details of Invasive Plant Populations. *Rangel. Ecol. Manag.* **2007**, *60*, 523–528. [CrossRef]
41. Zhang, C.; Kovacs, J.M. The application of small unmanned aerial systems for precision agriculture: A review. *Precis. Agric.* **2012**, *13*, 693–712. [CrossRef]